Comprehensive Radio – Frequency Ion Thruster Electromagnetic and Thermal Modelling

IEPC-2015-410／ISTS-2015-b-410

Presented at Joint Conference of 30th International Symposium on Space Technology and Science 34th International Electric Propulsion Conference and 6th Nano-satellite Symposium, Hyogo-Kobe, Japan July 4 – 10, 2015

Mantas Dobkevicius[1] and Davar Feili[2]
University of Southampton, Southampton, Hampshire, SO17 1BJ, United Kingdom

Johann Müller[3]
EADS Astrium GmbH, München, 801169, Germany

Abstract: A comprehensive radio-frequency gridded-ion thruster model is presented in order to investigate the main thruster performance parameters. The model is composed of various sub-models to account for different physics phenomena present during the thruster operation. A 2D axis-symmetric ion gun sub-model is used to determine the ion optics effective transparency and beam divergence. A 3D molecular gas sub-model calculates the neutral gas pressure and density in the discharge. An electron transport sub-model solves a two-term approximation Boltzmann equation to obtain rate coefficients and the effective collision frequency. A volume-averaged 0D plasma sub-model is employed to calculate the plasma density, temperature, potential and stochastic collision frequency. To improve on the uniform plasma assumption, a radial variation in plasma density/conductivity is introduced. The coupling between the coil and plasma is represented using a 2D axis-symmetric electromagnetic sub-model that solves Maxwell's equations in the plasma represented by a complex conductivity and surrounding thruster components. A 3D thermal sub-model calculates the temperature distribution inside the thruster. To account for the impedance matching and power losses within the cable and radio-frequency generator, a radio-frequency circuit sub-model is introduced with the thruster effect on the circuit expressed through a complex impedance obtained from the EM sub-model. It was shown that the model predicts the main RIT 3.5 thruster performance parameters within 10% error when compared to the experimental test data.

Nomenclature

A = area, m^2
B = magnetic field, T
D = electric displacement field, C/m^2
D_a = ion diffusion coefficient, m^2/s
C = capacitance, F
E = electric field, V/m
f_o = grid open area fraction
G = incident molecular flux, $1/(m^2 s)$

[1] Graduate Student, Department of Aeronautics & Astronautics, md4g09@soton.ac.uk.
[2] Senior Lecturer, Department of Aeronautics & Astronautics, D.Feili@soton.ac.uk.
[3] Retired, Electric Propulsion Engineer, Joh1mueller@aol.com.

h = local and center plasma density ratio
I = current, A
J = emitted molecular flux, $1/(m^2 s)$
k_f = field coupling coefficient
k_k = rate coefficient for collision species k, m^3/s
k = thermal conductivity, $W/(mK)$
L = inductance, H
M_i = ion mass, kg
$\widetilde{M}$ = complex mutual inductance, H
m_{asp} = asperities average slope, rad
$\dot{m}$ = gas flow rate, $sccm$
n = density, $1/m^3$
p = pressure, $mTorr$
P = power, W
R = resistance, Ohm
T_e = plasma temperature, eV
T_{eff} = effective ion optics transparency
T_0 = neutral gas temperature, K
T_w = discharge chamber wall temperature, K
U_i = ionization potential, eV
U = grid voltage, V
u_B = Bohm velocity, m/s
V = potential, V
v = velocity, m/s
W = energy, J
w = work function, eV
Z = complex impedance, Ohm
β = ionization fraction
Γ = particle current, $particles/s$
δ_B = ion confinement factor
δ_{eff} = effective skin depth, m
ε = mean electron energy, eV
η_c = Clausing factor
λ_i = ion mean free path, m
μ = electron mobility, $m^2/(Vs)$
ν = collision frequency, Hz
ρ_v = space charge density, C/m^3
σ_{asp} = asperities average height, m
σ_p = complex plasma conductivity, S/m
σ_k = collision cross section for species k, m^2
$\tilde{\sigma}_m$ = effective total momentum transfer collision cross-section, m^2
ϕ = plasma potential, V
χ_{01} = first zero of the Bessel function of the first kind
ω = radial frequency, Hz
$\mathcal{I}$ = stochastic heating parameter
$\mathcal{I}_1$ = Bessel function of the first kind
c = speed of light, 299 792 458 m/s
e = elementary charge, $1.619 \times 10^{-19}\ C$
g_0 = conversion factor from A to $sccm$ for Xenon, 13.938 $sccm/A$
m = electron mass, $9.10938291 \times 10^{-31}\ kg$
ε_0 = permittivity of free space, $8.85418782 \times 10^{-12}\ F/m$
$scrn$ = positively biased ion optics grid
$acel$ = negatively biased ion optics grid
$decel$ = ground potential ion optics grid

I. Introduction

The radio frequency (RF) ion thrusters (RIT) consist of a coil wrapped around an insulating gas chamber connected to a set of negatively biased high voltage ion extraction grids[1-4]. A typical RF ion thruster including the main physical processes and the radio-frequency generator (RFG) is shown in Fig. 1. An essential component of the thruster is the coil that is used to generate a sufficient electric field in order to ionize the gas inside the chamber, creating a high-density plasma. The coil is powered by an RFG that converts a DC voltage input signal to an AC output voltage signal V_g at a frequency in the range of 1 to 20 MHz. Between the RFG and coil, there is a coaxial cable and an impedance matching network. The aim when designing a thruster is to transfer as much power as possible from the RFG to the plasma. An ideal thruster, therefore, would transfer all input power to the plasma. However, a substantial amount of the power goes into the coil itself, the cable, the RFG and the surrounding thruster components. All these contribute to the losses and heating of the thruster. As can be seen, the RF thruster operation encompasses many different areas of physics, requiring a holistic modeling approach in order to accurately predict the behavior and performance of the thruster.

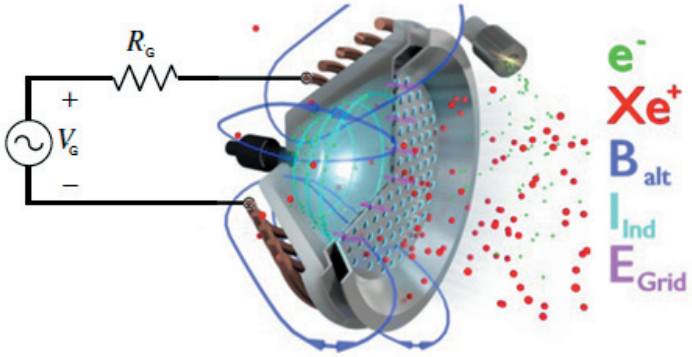

Figure 1. Main physical processes and components present in RF thrusters.
Picture adapted from Benjamin Lotz's Ph.D. Thesis[5].

So far developed RF inductive discharge models mainly used the volume-averaged (0D) plasma, as well as Maxwellian electron assumptions in order to determine the plasma properties. The coupling between the coil and plasma, and the power transferred from the coil to the plasma was estimated using what is known as the transformer method[6-11]. Furthermore, analytical Maxwell's equations were solved using an idealized coil and chamber geometries excluding skin, proximity and end-coil effects. In most case, the models also neglected the plasma power absorption dependency on the ion density and plasma conductivity spatial variation. Furthermore, only the plasma, chamber and coil were modelled; influence of the surrounding thruster components, for instance, the screen grid and case on the thruster performance was not taken into account. The few thermal models that were presented did not include the plasma effect on the thruster temperature, and the thruster temperature effect on the plasma properties and electromagnetic power losses[12]. Often the RF circuit effects were excluded from the thruster modelling analysis altogether.

Based on the aforementioned issues, a model that combines all aspect of RF thruster operation rather than concentrating on a specific area of physics has been developed. Each different type of physics is represented by a different sub-model designed in either COMSOL[13], PSpice[14] or Matlab[15]. First, the model determines the extracted ion current based on the upstream plasma properties which translate from the input mass flow rate and RFG voltage. In determining the plasma properties, the shape of the electron energy distribution function and the neutral gas molecular flow through the ion optics grids are accounted. The thruster-plasma system is represented by solving Maxwell's equations with the complex plasma conductivity set as a function of radius. From this analysis, the power transferred to the plasma and the power lost in the thruster are calculated. The power losses are used to determine the thruster temperature distribution. Finally, the RF circuit is constructed to determine the matching parameters and the power losses within the circuit and RFG, allowing the estimation of the total power needed to sustain the given discharge. The model is benchmarked against the experimental results of RIT 3.5 miniature RF thruster designed by Dr. Davar Feili for the Next Generation Gravity Mission (NGGM)[16].

II. Description of the model

The schematics description of the model is shown in Fig. 2. The models consists of different sub-models: 2D ion optics, 3D neutral gas, Boltzmann electron transport, 0D plasma, 2D electromagnetic (EM), 3D thermal and RF circuit. The ion optics, neutral gas, Boltzmann electron transport, EM and thermal models are created in COMSOL. Whereas, the 0D plasma and RF circuit models are constructed in Matlab and PSpice, respectively. All the sub-models are coupled together through Matlab to easily control the input variables and output parameters. The mass flow rate $\dot{m}_{in}$, RFG voltage V_{in} and the voltages on the grids U^+, U^- are given as the input parameters. The system is solved for two unknowns: electron temperature T_e and ion density n_i. At the beginning of each iteration, the guesses for these unknowns are passed together with the input parameters to the different sub-models. The output parameters from each sub-model are then used as inputs for the consecutive sub-models and so on. The first main output parameter is the plasma conductivity σ_p that is used in the EM sub-model to represent the thruster-plasma system. From the EM sub-model the coil current I_c, thruster resistance R_{thr} and thruster inductance L_{thr} are determined based on the plasma input parameters. The coil current together with the plasma power losses P_{loss} are then used in the thermal model to find the temperature distribution. Finally, the effective plasma-thruster system parameters R_{thr} and L_{thr} are used in the RF circuit sub-model to determine the impedance matching frequency and circuit losses. The system is solved as a global minimization problem in Matlab. The iterations are stopped when the total difference between the input electron temperature and RFG voltage becomes minimum.

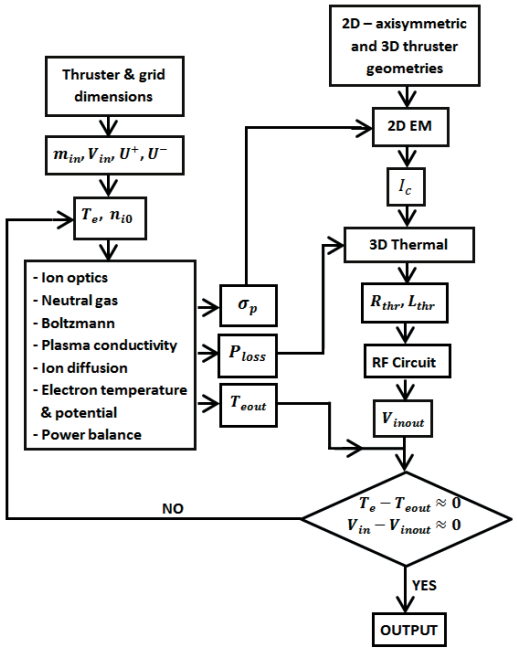

Figure 2. Solution method and main parameters of the model.

A. Ion optics sub – model

A 2D axis-symmetric ion optics sub-model has been developed using COMSOL based on the models from Ref. 17-19 in order to determine the beam properties. The model uses Maxwell's equations to calculate potentials from the electric field:

$$\begin{aligned} \Delta \cdot D &= \rho_v, \\ E &= -\Delta V, \end{aligned} \tag{1}$$

where ρ_v is the space charge due to ion n_i and electron n_e densities:

$$\rho_v = e(n_i - n_e). \tag{2}$$

The ion trajectories are obtained by solving an equation of motion based on the electric field distribution:

$$M_i \frac{dv_i}{dt} = -e\Delta V. \tag{3}$$

The plasma is represented using an upstream surface with the potential ϕ_0 given by:

$$\phi_0 = \phi_p + U^+, \tag{4}$$

where ϕ_p is the floating plasma potential, generally about 20-30 V, and U^+ is the screen grid potential. Ions are launched from this surface with the Bohm velocity u_B in order to mimic the pre-sheath behavior:

$$u_B = \sqrt{\frac{eT_{e0}}{M_i}}, \tag{5}$$

where T_{e0} is the upstream electron temperature. The electrons in the plasma sheath are modelled using a 1D Boltzmann relationship which states that the Maxwellian electron density n_e can solely be determined from the local potential ϕ and upstream plasma parameters:

$$n_e = n_{e0} \exp\left(\frac{\phi - \phi_0}{T_{e0}}\right), \tag{6}$$

where n_{e0} is the upstream plasma density.

In order to quantify the extracted beam current, the effective transparency of the ion optics system T_{eff} is calculated as the ratio of the extracted ion beam current I_b to the total ion current flowing towards the grids I_i:

$$T_{eff} = {I_b}/{I_i}. \tag{7}$$

The solution is obtained by first calculating the electric potentials due to the grids and plasma potential ϕ_0. Ions are then injected with a Bohm current density based on the upstream plasma conditions and tracked through the system assuming that the potentials are not influenced by the space charge left behind by the ions and electrons. Once the ions have reached the end of the simulation domain, the fields are updated to account for the change in the space charge. The process is repeated until a steady state is reached, that is, the fields and ion trajectories stop changing with time. The upstream ion density n_{i0} is increased in small increments δn_{i0} up to the desired ion density for a better convergence. An example of ion beam trajectories and potentials, as predicted by the model for a set of RIT 3.5 grids, is shown in Fig. 3.

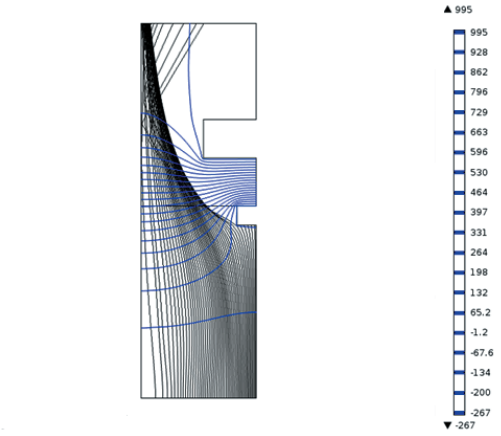

Figure 3. Potential distribution and ion trajectories for the RIT 3.5 ion optics grids and $U^+ = 1\ kV$.

B. Neutral gas sub – model

First, a 2D axis-symmetric free molecular flow sub-model is constructed in COMSOL that is used to determine the gas molecule transmission probability through the ion optics. This probability is commonly referred to as the Clausing factor η_c[20]. In COMSOL it is calculated as the ratio of the incident molecular flux G integrated over the surface of the screen aperture divided by the emitted molecular flux J integrated over the decel grid aperture surface:

$$\eta_c = {\int G \cdot dr}/{\int J \cdot dr}. \tag{8}$$

An example of the neutral gas distribution in the RIT 3.5 ion optics is shown in Fig. 4. Next, the Clausing factor is passed to a 3D free molecular flow COMSOL sub-model. The sub-model takes into account the actual discharge chamber, inlet aperture and screen grid dimensions.

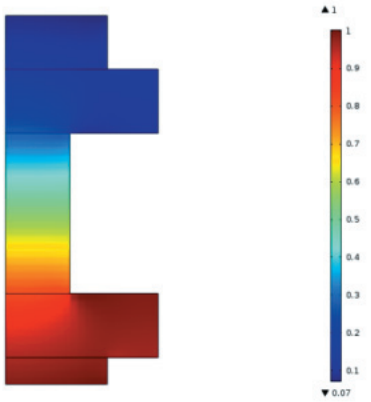

Figure 4. Neutral gas density distribution normalized to the upstream value inside the RIT 3.5 ion optics.

In order to calculate the neutral gas pressure p_0 and density n_0 inside the chamber, the amount of neutral gas that leaks through the grids $\dot{m}_{out}$ and is not part of the ion beam is estimated. This is used as the neutral gas input mass flow rate for the sub-model. It is calculated by simply subtracting the equivalent mass flow rate required to obtain a specific ion beam current I_b from the input mass flow rate $\dot{m}_{in}$ as given by the following equation:

$$\dot{m}_{out} = \dot{m}_{in} - I_b \cdot g_0, \tag{9}$$

where g_0 is the conversion factor from A to $sccm$ equal to 13.938 $sccm/A$.

A boundary condition is applied on the screen grid apertures that reflects a fraction of incident molecules G back to the discharge chamber. The fraction is expressed through the Clausing factor as:

$$J = (1 - \eta_c)G. \tag{10}$$

The model also includes the effects of discharge chamber temperature T_w on the neutral gas pressure and density. Figure 5 shows an example of the neutral gas density distribution in the chamber normalized to the maximum value.

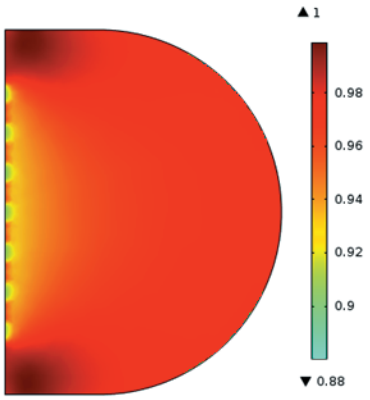

Figure 5. Neutral gas density distribution normalized to the maximum value in the RIT 3.5 discharge chamber. *Darker regions represent the areas where the gas enters the chamber (top left and right corners of the discharge). Brighter regions indicate lower density areas (left side of the chamber), especially obvious near the grid apertures. In general the neutral density is quite uniform, only around 10% in variation.*

C. Electron transport sub – model

It was shown in Ref. 21 that it is very important to account for oscillating fields and the shape of the electron energy distribution function (EEDF) while calculating high-frequency (HF) plasma properties. Therefore, a two-term approximation Boltzmann equation for oscillating fields[22] is solved using COMSOL as a function of the reduced electric field (E_0/n_0) and angular frequency (ω/n_0) based on the collision cross-section data taken from Ref. 23:

$$-\frac{\gamma}{3}\frac{\partial}{\partial\varepsilon}\left(\left(\frac{E_0}{n_0}\right)^2\frac{\tilde{\sigma}_m\varepsilon}{2(\tilde{\sigma}_m^2+q^2)}\frac{\partial F_0}{\partial\varepsilon}\right)=\tilde{C}_0+\tilde{R}, \tag{11}$$

where $\tilde{C}_0$ and $\tilde{R}$ are collision and growth renormalization terms, respectively, $\tilde{\sigma}_m$ is the effective total momentum transfer collision cross-section, ε is the average electron energy, $\gamma=\sqrt{2e/m}$ and $q=\omega/\left(n_0\,\gamma\sqrt{\varepsilon}\right)$. F_0 is a normalized EEDF given as:

$$\int_0^\infty\sqrt{\varepsilon}F_0d\varepsilon=1. \tag{12}$$

The electron mobility μ is calculated as[22]:

$$\mu=-\frac{\gamma}{3n_0}\int_0^\infty\frac{\varepsilon}{\tilde{\sigma}_m}\frac{\partial F_0}{\partial\varepsilon}d\varepsilon. \tag{13}$$

Then the effective electron neutral collision frequency ν_{eff} is obtained as:

$$\mu=\frac{e/m}{\nu_{eff}+j\omega_{eff}}, \tag{14}$$

where it is assumed that the effective angular frequency ω_{eff} is approximately equal to the applied angular frequency ω. It is an accurate assumption considering the pressure range that RIT 3.5 operates[21]. The rate coefficient k for each collision process k is found as:

$$k_k=\gamma\int_0^\infty\varepsilon\sigma_kF_0d\varepsilon. \tag{15}$$

Using the previously calculated rate coefficients, the reaction rate for the collision process between two species with densities N_1 and N_2 is:

$$R_k=k_kN_1N_2. \tag{16}$$

Additionally, the neutral gas temperature T_0 which is assumed equal to the chamber wall temperature T_w and ionization fraction β are given as inputs to the sub-model:

$$\beta=\frac{n_{i0}}{n_{i0}+n_0}. \tag{17}$$

Figures 6 and 7 show examples of EEDFs plotted up to the maximum electron energy of $100\ eV$ based on different ionization fractions β and reduced angular frequencies (ω/n_0) typical to RIT class ion thrusters for a mean electron energy of $6\ eV$. Note that the more the curve approaches the shape of a straight line, the more it resembles the Maxwellian distribution. It has been shown that as the ionization degree β increases, the electron-electron collision tend to drive the distribution towards Maxwellian[22]. The RIT type thrusters operate in quite a high-density regime with a high ionization fraction. Therefore, the EEDF encountered should be close to the Maxwellian at low energies. However, as can be observed in Fig. 6 the tail of the distribution is considerably different from the Maxwellian (straight line).

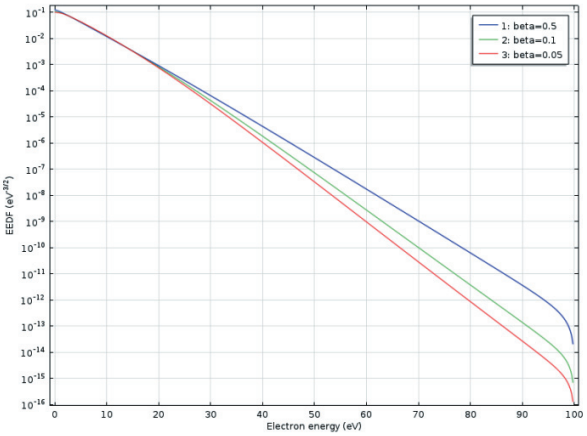

Figure 6. EEDF for different ionization degrees for the mean electron energy of 6 eV.
Three different ionization degrees are: $\beta = 0.5$, $\beta = 0.1$ and $\beta = 0.05$.

Figure 7 shows that the EEDF for a DC case is substantially different from the AC cases 1 and 2, especially at higher electron energies. It reinforces our reasoning that the effective collision frequency ν_{eff} must be solved using the high-frequency (HF) electron mobility μ. It comes from the fact that the heating mechanism in DC and HF fields is different. Namely, in DC fields the collisions impede the heating process, while in HF fields they enhance it[22]. That is why we see a higher number of more energetic electrons for HF case than DC case in the tail of the distribution.

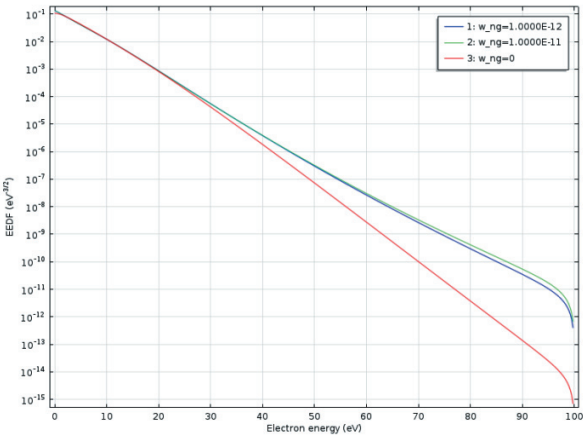

Figure 7. EEDF for different reduced angular frequencies for the mean electron energy of 6 eV.
Three different reduced angular frequencies are: $\omega/n_0 = 10^{-12}$, $\omega/n_0 = 10^{-11}$ and $\omega/n_0 = 0$ (DC).

D. Plasma sub – model

1. Ion diffusion

It has been observed that in order to accurately account for the plasma electromagnetic heating, the ion density distribution is extremely important. From RIT 10 ion density measurements and from the literature it was discovered that the ion density varies as a function of the radial distance from the discharge vessel center[24]. We introduce this variation in density through the h parameter:

$$h = \frac{n(r)}{n(0)}, \tag{18}$$

where $n(0)$ is the ion density at the center of the discharge and $n(r)$ is the ion density at a location r from the center.

We often speak of an h_r parameter which is the ion density ratio at $r = R$ location. Lieberman and Lichtenberg derived the following expression for estimating the ion density profile as a function of the radial distance r for low pressure discharges[6]:

$$\left(\frac{n}{n_0}\right)^2 + \left(\frac{r}{R}\right)^2 = 1. \tag{19}$$

It is simply an equation of a circle with the ion density equal to n_0 at the center and zero at the radial edge boundary. However, it was discovered that the ion density profile varies depending on the pressure, size of the system, magnetic field, etc. Therefore, a more general solution was derived to estimate the h_r parameter[6]:

$$h_r = \frac{0.8}{\left[4 + \frac{R}{\lambda_i} + \left(0.8Ru_B/(\chi_{01}\mathcal{J}_1(\chi_{01})D_a)\right)^2\right]^{1/2}}, \tag{20}$$

and introducing h_l value to account for the ion density variation in the axial l direction:

$$h_l = \frac{0.86}{\left[3 + \frac{l}{2\lambda_i} + \left(0.86lu_B/(\pi D_a)\right)^2\right]^{1/2}}, \tag{21}$$

where D_a is the ion diffusion coefficient and λ_i is the ion mean free path.

However, it was found that the circular ion density profile defined in Eq. (19) is still approximately correct. Therefore, it was still used, but modified to account for the h_r factor at the wall and the plasma sheath thickness s as given below:

$$h = \sqrt{1 - \left(\sqrt{1 - h_r^2}\frac{r}{R - s}\right)^2}. \tag{22}$$

Figure 8 compares the ion density variation as measured in RIT 10 thruster[24] and the model prediction up to the plasma sheath assuming $h_r = 0.39$, which is a reasonable value for such a discharge considering that RIT 10 operates at around 1 $mTorr$ of pressure.

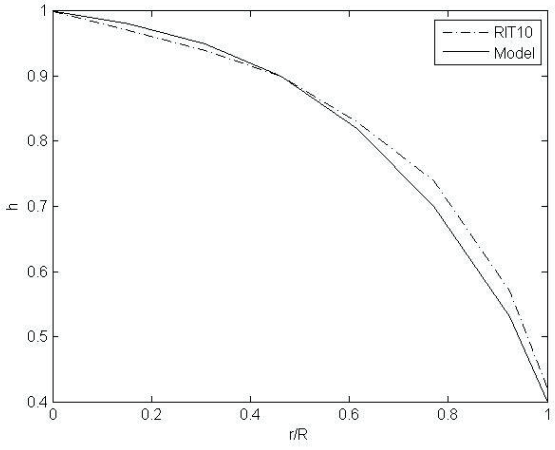

Figure 8. Ion density variation with radial distance as measured in RIT 10 and predicted by the model[24].

Figure 9 shows the plasma density variation for RIT 3.5 thruster setting the sheath size s equal to 2 mm and h_r to 0.5. Downstream of the sheath edge it is assumed that the ion density follows a parabolic distribution and drops sharply to zero at the wall.

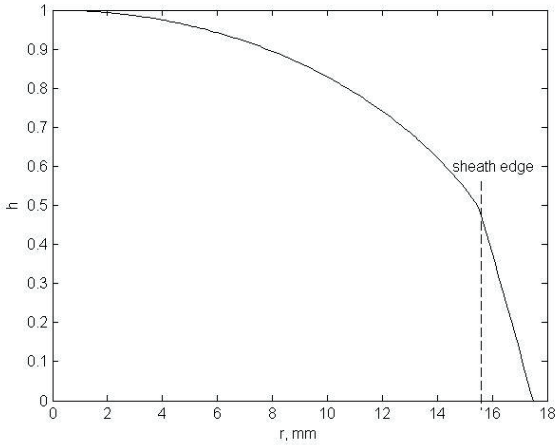

Figure 9. Ion density variation and the location of the sheath edge for RIT 3.5 thruster.

The h_r and h_l parameters greatly depend on the pressure through the ion mean free path λ_i. As can be seen in Fig. 10, in the range of RIT 3.5 working pressures from 0.1 to 1 $mTorr$ both coefficients are about constant. However, if the pressure is increased above 1 $mTorr$, they start to drop sharply.

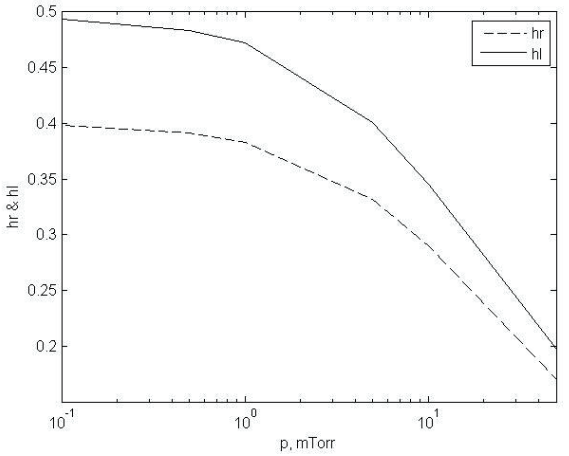

Figure 10. h_r and h_l parameter variation with neutral gas pressure for RIT 3.5 thruster.

Some authors[11] have speculated that the magnetic field results in an ion confinement and, thus, lower losses to the boundaries. It was decided to investigate this phenomenon through the ion diffusion since the pre-sheath ion density values h_r and h_l directly depend on the ion diffusion coefficient D_a, which in turn depends on the magnetic field. The reduction of h_r and h_l parameters would directly lead to lower boundary losses and, therefore, better plasma confinement. In a special case of an ambipolar diffusion across a uniform magnetic field, D_a coefficient is[8]:

$$D_a^* = \frac{kT_e}{M\nu_i}(1+\delta_B)^{-1}. \tag{23}$$

The δ_B parameter can be considered as a confinement factor since it strongly depends on the magnetic field through:

$$\delta_B = \frac{\omega_{ci}\omega_{ce}}{\nu_i\nu_e}, \tag{24}$$

where ν_i and ν_e are ion and electron collision frequencies with neutrals, whereas ω_{ci} and ω_{ce} are ion and electron cyclotron frequencies, respectively:

$$\omega_c = \frac{eB}{M_i}. \tag{25}$$

It should be noted that this analysis is for a steady magnetic field. There are two possible approximations in order to deal with an AC field. One is to consider the RMS value of the AC magnetic field. The other one is to use the effective magnetic field B_{eff} value given by some authors as[22, 25]:

$$B_{eff} = \frac{B_0}{\sqrt{2}\sqrt{1+\omega^2/\nu^2}}. \tag{26}$$

Since the ω/ν ratio for RIT 3.5 operational conditions is approximately equal to one, it was decided to simply use the RMS value of the magnetic field. As Fig. 11 indicates, for RIT 3.5 thruster, the magnetic field starts to become significant only from about 400 $Gauss$ for 1 $mTorr$ case, and from about 100 $Gauss$ for 0.1 $mTorr$ case. However, the maximum magnetic field expected in the RIT 3.5 plasma is only about 20 $Gauss$, and the magnetic field distribution is not uniform, decreasing sharply away from the coil, as can be observed in Fig. 12.

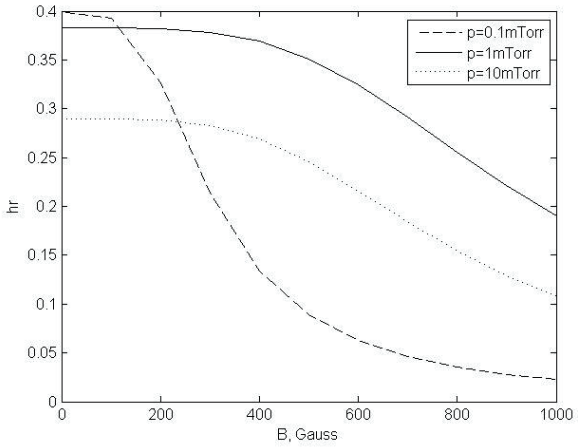

Figure 11. h_r parameter variation with the magnetic field for three different neutral gas pressures.

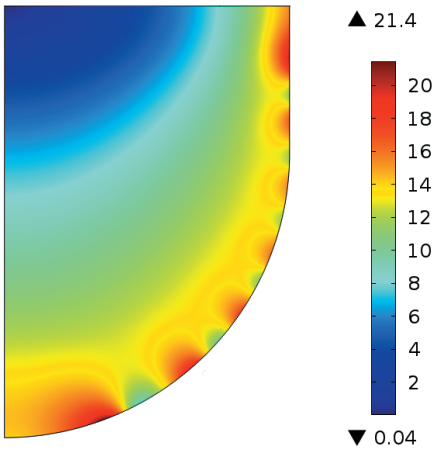

Figure 12. Magnetic field in $Gauss$ inside RIT 3.5 plasma for 2.5 mN thrust operational condition.

2. Plasma conductivity

The plasma acts much like an ordinary conductor and can be represented using familiar properties generally used to define conductors. The first of these is a plasma conductivity. Neglecting the displacement current, the plasma conductivity can be represented as[25]:

$$\sigma_p = \frac{n_i e^2}{m_e(\nu_{tot} + i\omega_{eff})}, \tag{27}$$

where ν_{tot} is the total collision frequency composed of different collision frequencies associated with various heating mechanisms. First, we will consider an electron-ion collision heating mechanism which is given by:

$$\nu_{ei} = 2.91 \times 10^{-12} \frac{n_i \ln\Lambda}{T_{e0}^{3/2}}, \tag{28}$$

and $\ln\Lambda$ is the Coulomb logarithm:

$$\ln\Lambda = 23 - 0.5 \ln \frac{10^{-6} n_i}{T_{e0}^3}. \tag{29}$$

Some authors observed that at low pressures collisional heating is not the dominant process, but rather what is called a stochastic heating dominates[26,27]. This happens because if an electron traverses a localized skin layer faster than the RF period, then it gains energy from the field[6,8]. In such a case, the spatial distribution of the electric field and current is not the usual exponential decay within the skin depth[6,8]. To deal with this some authors have defined an anomalous skin depth δ_{eff} which estimates an effective skin penetration length[8]:

$$\delta_{eff} = \left(\frac{v_e c^2}{\omega \omega_{pe}^2}\right)^{1/3}, \tag{30}$$

where

$$\omega_{pe} = \sqrt{n_{i0} e^2 / m\varepsilon_0}. \tag{31}$$

Lieberman and Lichtenberg have introduced an equivalent stochastic frequency to represent the stochastic heating mechanism[6]:

$$\nu_{stoc} = \frac{v_e}{4\delta_{eff}} \left(\frac{1}{\mathcal{I}(\alpha) + \alpha/4}\right), \tag{32}$$

where $\mathcal{I}(\alpha)$ is:

$$\mathcal{I}(\alpha) = \frac{1}{\pi}\left[e^{\alpha}(1+\alpha)\int_{\alpha}^{\infty} d\xi \frac{e^{-\xi}}{\xi} - 1\right], \tag{33}$$

and

$$\alpha = \frac{4\omega^2 \delta_{eff}^2}{\pi v_e^2}, \tag{34}$$

where $\xi = m v_e^2/(2eT_e)$. Finally, the total collision frequency ν_{tot} can be determined as the sum of the effective collision frequency ν_{eff}, electron-ion collision frequency ν_{ei}, and stochastic collision frequency ν_{stoc}:

$$\nu_{tot} = \nu_{eff} + \nu_{ei} + \nu_{stoc}. \tag{35}$$

3. Electron temperature and potential

The electron temperature is found using a particle balance of ions by setting the rate of ion loss equal to the rate of ion production. For the ion loss, it is assumed that ions flow to the walls with the Bohm velocity and upon reaching them recombine to produce a neutral atom, except those ions that are extracted to the beam. Ion production, on the other hand, is expressed using Eq. (16) with ion and neutral gas densities, and ionization rate constant k_i. After some manipulation the final equation is:

$$n_0 k_i(T_e) V = u_B(h_r A_w + h_l A_s). \tag{36}$$

The plasma potential is obtained by assuming that the electron and ion fluxes to the boundaries are ambipolar or equal. Therefore, the floating plasma potential is given by a well-known equation:

$$\phi = T_e \ln \sqrt{M_i/(2\pi m)}\,. \tag{37}$$

4. Power losses

In order to account for the plasma's effect on the thruster heating, the particle currents within the discharge chamber are determined. Using the conservation of particles and energy, the total ion current in particles per second flowing towards the discharge chamber wall is:

$$\Gamma_{wi} = h_r n_{i0} u_B A_w. \tag{38}$$

Since the flow is assumed to be ambipolar, the electron current to the wall Γ_{we} is equal to the ion current Γ_{wi}. The ion current to the screen grid is equal to the remaining current that is not extracted through the grids to form the ion beam:

$$\Gamma_{si} = (1 - T_{eff}) h_l n_{i0} u_B A_s. \tag{39}$$

Assuming ambipolar losses again, the electron current to the screen grid is:

$$\Gamma_{se} = \Gamma_b + \Gamma_{si}, \tag{40}$$

where Γ_b is the ion beam current in particles per second. There are two main mechanisms by which the chamber is heated. First is due to the energy deposited to the walls gained by particles crossing electric fields in the plasma sheath. The other one is due to the radiation from excited neutrals[28]. To account for the radiative heating, we assume that each surface gets a fraction of the total radiative power depending on its relative size. First, the chamber heating due to the ion and electron currents is:

$$P_c = \Gamma_{wi}\left(\phi + \frac{5}{2}T_e + U_i\right), \tag{41}$$

where U_i is the ionization potential. The chamber heating due to the excited neutrals is:

$$P_{xc} = \frac{A_c}{A_w} P_x, \tag{42}$$

where P_x is the total power lost to excitation of the neutral gas. The screen grid heating due to electrons is:

$$P_{se} = \Gamma_{se}(w_s + 2T_e), \tag{43}$$

where w_s is the screen grid work function. Whereas, the screen grid heating due to ions is:

$$P_{si} = \Gamma_{si}\left(\phi + \frac{1}{2}T_e + U_i - w_s\right). \tag{44}$$

Finally, the screen grid heating due to excited neutrals is:

$$P_{xs} = \frac{(1 - f_{os})A_s}{A_w} P_x, \tag{45}$$

where f_{os} and f_{oa} represent the screen and acel grid open area fractions, respectively. The heating of the acel grid comes mainly from the excited neutral radiation:

$$P_{xa} = \frac{(1 - f_{oa})f_{os}A_s}{A_w} P_x, \tag{46}$$

and charge exchange (CEX) ions:

$$P_{CEX} = \Gamma_a(U^- + U_i - w_a), \tag{47}$$

where Γ_a is the CEX particle current, usually less than 2% of the beam current, and w_a is the acel grid work function. The power processed by the RFG power supply also includes the excited neutral radiation power that escapes through the grid system:

$$P_{xout} = \frac{f_{oa}f_{os}A_s}{A_w} P_x, \tag{48}$$

and the power that escapes with the ions in the beam:

$$P_b = \Gamma_b \left(\phi + \frac{1}{2}T_e + U_i\right). \tag{49}$$

The total power P_0 that is needed to generate the required density plasma at a specified mass flow rate is a sum of all the aforementioned losses:

$$P_0 = P_c + P_{xc} + P_{se} + P_{si} + P_{xs} + P_{xa} + P_{xout} + P_b. \tag{50}$$

E. RF circuit sub – model

The coil, plasma and the surrounding thruster components can be transformed through the Maxwell's equations to an equivalent circuit as shown in Fig 13. The transformation depends on the coupling coefficient k, component resistance R and inductance L. Note that the plasma has an additional inductance L_p coming from the complex nature of plasma conductivity. This complex part introduces a phase lag between the voltage and current[6]. The final equivalent system has only two components: the thruster resistance R_{thr} and inductance L_{thr}.

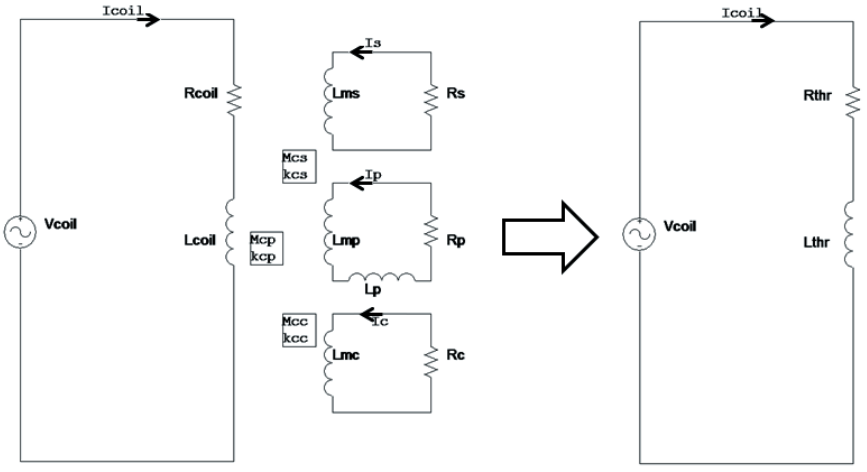

Figure 13. Thruster impedance transformation network (left) and equivalent thruster representation (right). The subscripts "s", "p" and "c" stand for the screen, plasma and case, respectively.

The complete schematics of an RF circuit is shown in Fig. 14. It is composed of an RFG, a coaxial cable and a thruster. The coaxial cable connecting the RFG and the thruster is represented by a "lossy" transmission line property in PSpice. There are also two impedance transformation capacitors C_1 and C_2. These capacitors cancel the predominantly inductive reactance of the circuit so that the RFG operates at a predefined frequency in a resonance mode; the phase angle of the circuit is zero. For RIT 3.5, the resonance frequency is around 3 MHz. Furthermore, the thruster resistance R_{thr} and inductance L_{thr} change during the operation. Therefore, the RFG works by adjusting the applied frequency in a phase controlled loop to keep the circuit in resonance. Additionally, the RFG is supplied with a DC voltage V_{in} and outputs an HF rectangular voltage waveform V_{out}. Finally, the input voltage V_{in} and input current I_{in} are used to determine the RFG input power.

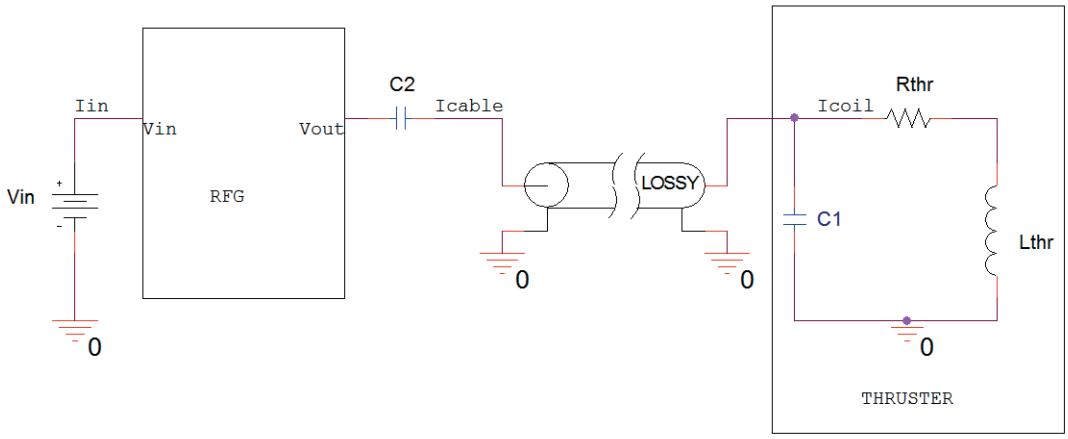

Figure 14. Simplified RF circuit with a thruster, coaxial cable and RFG.
The thruster is represented with R_{thr} and L_{thr} parameters.

F. EM sub – model

A 2D axis-symmetric electromagnetic model has been created in COMSOL in order to solve the Maxwell's equations in the plasma and thruster. The model treats the plasma as a simple solid with a complex conductivity determined from Eq. (27) and given here as:

$$\sigma_p = \sigma_r - \sigma_i \cdot j. \tag{51}$$

Representing the plasma conductivity in such a way introduces a phase lag between the electric field and current in order to account for the finite electron inertia[8]. This is done to mimic the actual behavior of the plasma. However, since the plasma conductivity directly depends on the ion density, it is very important to account for the spatial variation of the plasma conductivity as well. It was discovered that the correct modelling of the plasma conductivity is essential in determining the power transferred from the coil to the plasma. In the proposed model, the plasma conductivity is represented using the following relationship:

$$\sigma_p \sim h n_{i0}. \tag{52}$$

It states that the plasma conductivity is directly proportional to the ion density distribution through the h parameter discussed earlier. For RIT 3.5 thruster, the plasma density and conductivity distribution is shown in Fig. 15. As can be seen, the ion density is highest near the central axis of the chamber and drops sharply to zero towards the wall boundaries. There is also a density variation in the axial direction, but this is not so important since the EM fields are screened by the plasma at the radial edge of the chamber.

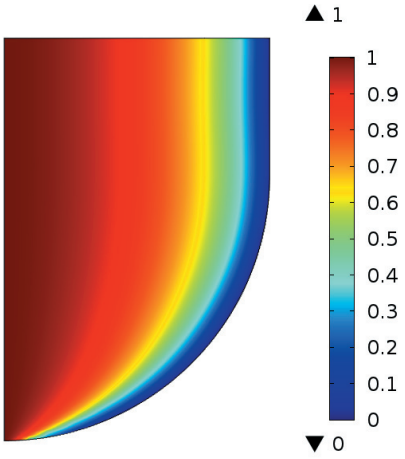

Figure 15. Plasma density variation normalized to the centre value in RIT 3.5 thruster for $h_r = 0.4$.

The complex thruster impedance is obtained directly from COMSOL as:

$$Z = R + jX. \tag{53}$$

The real part R of the complex impedance represents the thruster's resistance and is associated with the actual power loss, whereas the complex part X represents the reactive component, or the phase lag as a result of inductive and capacitive couplings. The inductance L and capacitance C are obtained from the magnetic W_m and electric W_e energies, respectively:

$$\begin{aligned} C &= \frac{4 \times W_e}{V^2}, \\ L &= \frac{4 \times W_m}{I^2}, \end{aligned} \tag{54}$$

where V and I are the coil voltage drop and coil current, respectively. The power lost in the thruster components and plasma is obtained using the following equation:

$$P_{abs} = \pi \iint \Re\left(\sigma_p * {E_\theta}^2\right) r dA, \tag{55}$$

where E_θ is the azimuthal electric field. The area-averaged potential voltage drop over plasma is given by:

$$\tilde{V}_p = \frac{\iint E_\theta 2\pi r \, dA}{A_p}, \tag{56}$$

where the tilde symbol represents the complex nature of the variable and A_p is the cross-sectional surface area of the plasma. The mutual inductance $\tilde{M}$ between the plasma and the coil, and the plasma geometrical inductance L_{mp} are obtained by solving Maxwell's equations in the thruster-plasma system:

$$\begin{aligned} \tilde{M} &= \left(\tilde{V}_{thr} - j\omega L_{thr}\tilde{I}_{coil} - R_{thr}\tilde{I}_{coil}\right)/j\omega\tilde{I}_p, \\ L_{mp} &= \left(\tilde{V}_p - j\omega\tilde{M}\tilde{I}_{coil}\right)/j\omega\tilde{I}_p. \end{aligned} \tag{57}$$

Finally, we define the field coupling coefficient k_f between the coil and plasma as:

$$k_f = \frac{M}{\sqrt{L_{mp}L_{thr}}}, \tag{58}$$

and the Q factor of the thruster as:

$$Q = \frac{\omega L_{thr}}{R_{thr}}. \tag{59}$$

G. Thermal sub – model

A 3D thermal thruster model has been designed in COMSOL by solving a steady state heat equation in order to obtain the temperature distribution:

$$\nabla(-k\nabla T) = Q_i, \tag{60}$$

where Q_i represents the heat sources within the system and k is the thermal conductivity. The thermal model has been designed in order to observe the temperature effect on the electromagnetic heating losses in the conductors. Furthermore, a thermal model is needed to analyze and help solve any potential thermal issues with regards to the impedance matching capacitor C_1 since it is recommended that its temperature does not increase above 150 ℃. Additionally, it has been decided to investigate the effect the temperature has on the gas pressure. Finally, the temperature distribution on the grids is used to perform further studies with regards to grid thermal deformation and stability.

There are two types of heat sources in the RF thruster, excluding the outside environment. The first heat source Q_{EM} is due to the EM heating, and is expressed only as a function of the coil current I_c and reflected component resistance R_i calculated from the EM sub-model:

$$Q_{EM} = 0.5R_i(T)I_c^2. \tag{61}$$

Figure 16 shows how the reflected coil resistance R_i varies with temperature.

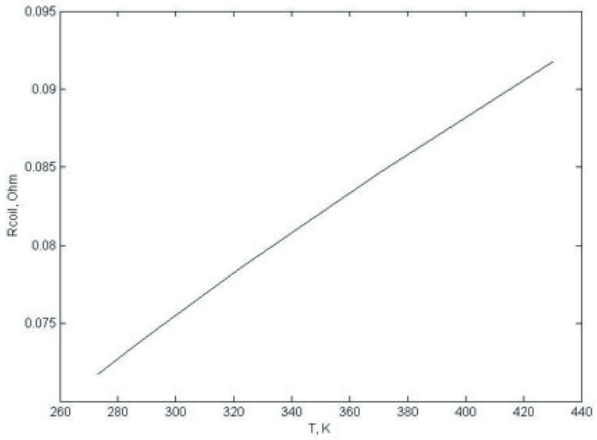

Figure 16. Reflected coil resistance R_i variation with temperature for RIT 3.5 thruster.

The other heat sources come from the plasma losses as discussed in section D. 4. To complete the thermal model, surface-to-surface and ambient radiation are included:

$$Q_{rad} = \varepsilon(G - \sigma T^4), \tag{62}$$

where ε is the emissivity of the material which is set equal to the absorptivity α due the grey-body assumption. The G parameter is the incoming heat flux composed of the ambient G_{amb} and mutual flux between the components G_m:

$$G = G_m + G_{amb}. \tag{63}$$

In order to save computational time, radiation groups are defined as well. This means that only components that have considerably large view factors are included in a particular radiation group. Furthermore, as shown in Fig. 17, the actual RIT 3.5 thruster grid geometry having 121 apertures has been replaced with the one having only 19 apertures, but the same open area fraction as the original.

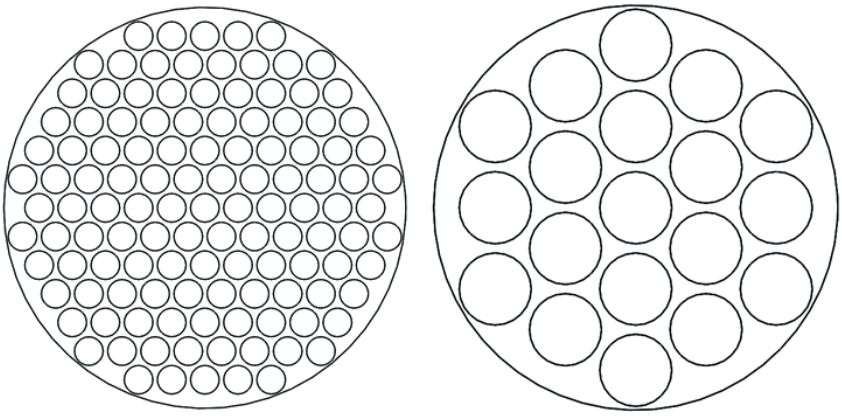

Figure 17. Equivalent screen grid representation in the thermal modelling.
Left: the actual RIT 3.5 screen grid with 121 apertures. Right: an equivalent screen grid with only 19 apertures, but with the same open area fraction.

Finally, Mikic's elastic model is used to account for the contact resistance between the adjacent surfaces:

$$h_c = 1.54 k_c \frac{m_{asp}}{\sigma_{asp}} \left(\frac{\sqrt{2} p_c}{m_{asp} E_c} \right)^{0.94}, \tag{64}$$

where m_{asp} and σ_{asp} are the effective RMS contact surface asperities slope and roughness, respectively, and k_c is the average conductivity of the surfaces with thermal conductivities k_1 and k_2 in contact:

$$k_c = \frac{2 k_1 k_2}{k_1 + k_2}. \tag{65}$$

The equivalent contact elastic modulus E_c is calculated using the elastic modulus E_1 and E_2, as well as Poisson's ratios ν_1 and ν_2 of the surfaces 1 and 2 in contact:

$$\frac{1}{E_c} = \frac{1 - \nu_1^2}{E_1} + \frac{1 - \nu_2^2}{E_2}. \tag{66}$$

III. Results

The results from the model are compared to the preliminary measurements of RIT 3.5 thruster using Xenon. As can be seen from Table 1, the errors in the model and experimental input currents I_{in} are between 7% and approximately 1.5%, while the errors for the input powers P_{in} are in the range of 6% to 0.5%. Since the errors are generally below 10%, the model is deemed accurate enough to be trusted. Note that the input power P_{in} refers to the RFG input power, and not the total power which also included the beam power supply power. In Fig. 18, the thruster input power is mapped for different mass flow rates as a function of the mass utilization efficiency given as $\eta_m = I_b g_0 / \dot{m}_{in}$. It can be seen that the input power starts to increases exponentially as the mass utilization efficiency goes above 0.65.

$\dot{m}_{in}, sccm$	η_m	$I_{in}\ Exp., A$	$I_{in}\ Mod., A$	$I_{in}\ Err., \%$	$P_{in}Exp., W$	$P_{in}Mod., W$	$P_{in}Err., \%$
0.20	0.17	1.34	1.41	-5.36%	7.95	7.50	5.69%
0.20	0.23	1.37	1.46	-6.86%	8.66	8.40	3.04%
0.20	0.34	1.45	1.53	-5.83%	10	10.5	4.76%
0.30	0.62	1.60	1.63	-1.69%	15.44	16.2	4.70%
0.47	0.75	2.00	2.10	-5.12%	28.06	29.20	-4.05%
0.50	0.75	1.92	1.95	-1.42%	26.67	26.00	2.52%
0.60	0.74	1.88	1.93	-2.93%	27.21	27.40	-0.70%
0.74	0.72	1.81	1.88	-4.07%	27.84	27.5	1.24%

Table 1. Comparison between the model and experimental results for RIT 3.5 thruster.
Exp., Mod. and Err. stand for experimental data, model result and the relative difference between experimental and model results, respectively.

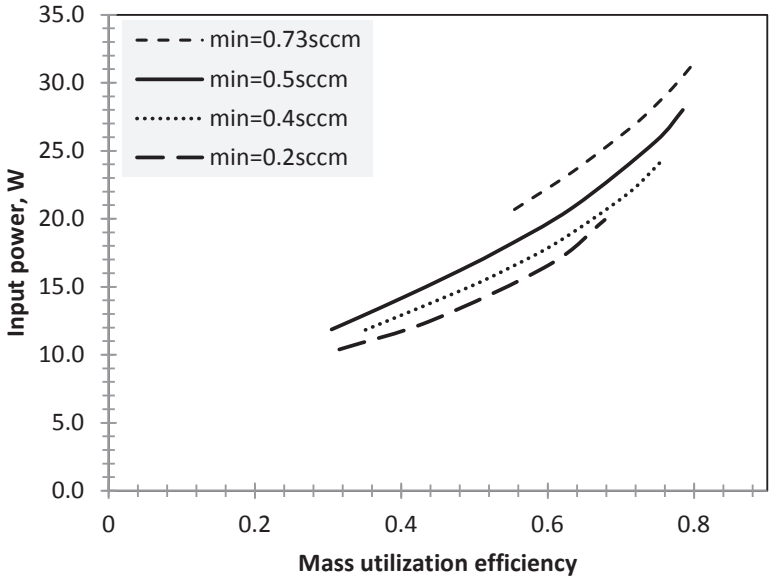

Figure 18. Input power as a function of the mass utilization efficiency for different input mass flow rates.

Figure 19 shows that as the input power increases, the ion density increases as well until it plateaus at the input power of around 20 W, while the neutral density decreases at a constant rate. Figure 20 indicates that the power transfer efficiency η_w plateaus, together with ion density, at around 0.65 at 20 W of input power, whereas the mass utilization efficiency η_m still keeps increasing up to 0.8 at 25 W of input power.

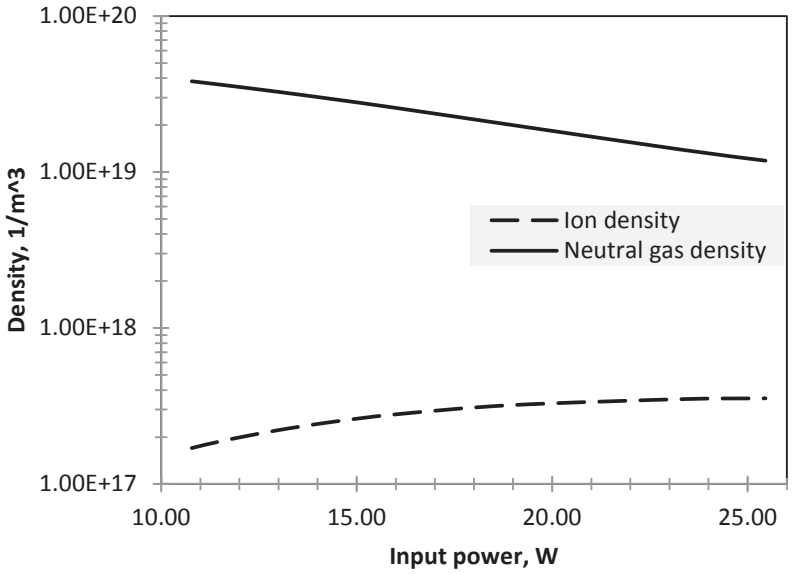

Figure 19. Neutral gas and ion densities as a function of the input power at $0.5\ sccm$ input mass flow rate.

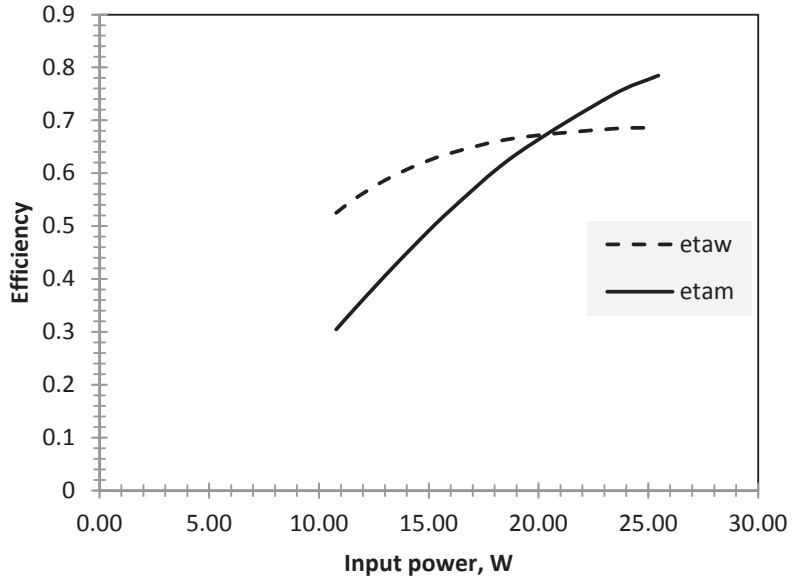

Figure 20. Thruster mass utilization efficiency (etam) and power transfer efficiency (etaw) as a function of the input power at $0.5\ sccm$ input mass flow rate.

As can be seen in Fig. 21, the thrust increases with the input power in almost a linear fashion, and reaches about $2.7\ mN$ at the input power of $32\ W$. Figure 22 shows that the thruster resistance R_{thr} plateaus, together with the ion density, to about $0.6\ Ohm$ at $20\ W$ of input power. Whereas, the plasma resistance R_p keeps sharply decreasing up to around $0.9\ Ohm$ at $20\ W$ of input power and then, again, starts to plateau. The plasma current I_p increases up to $4.2\ A$ at around 22 W of input power, before starting to level off.

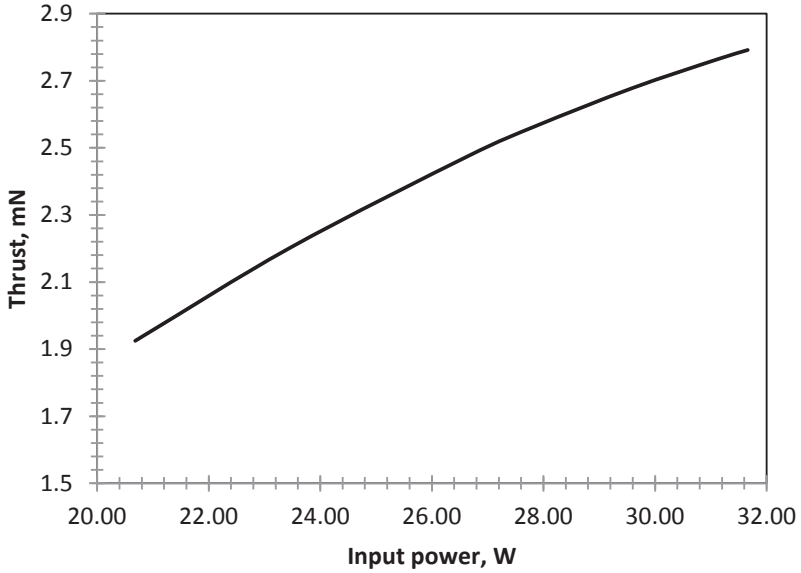

Figure 21. Thrust as a function of the input power at 0.73 $sccm$ input mass flow rate.

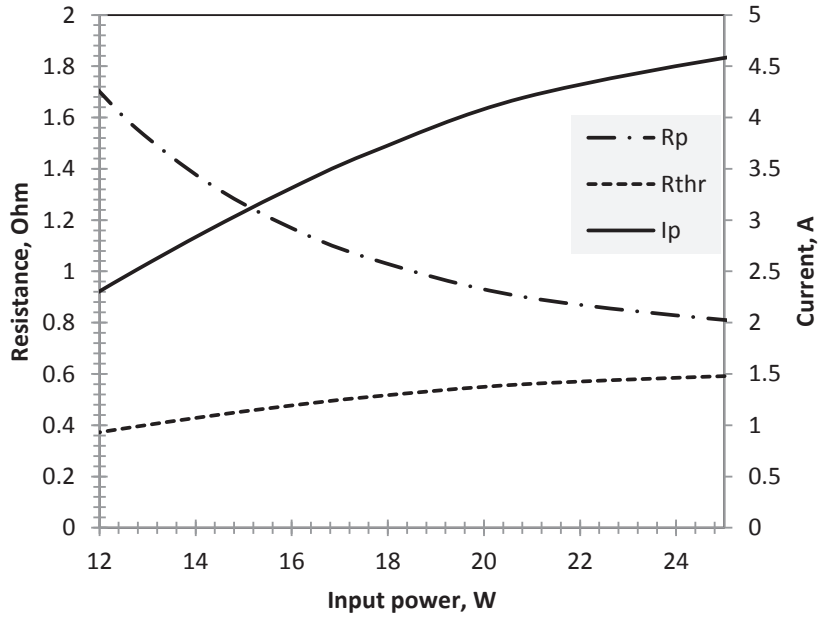

Figure 22. Thruster resistance, plasma resistance and plasma current as a function of the mass utilization efficiency at 0.5 $sccm$ mass input flow rate.

From Fig. 23 it can be inferred that the coupling factor for RIT 3.5 varies between 0.15 at the mass flow rate of 0.2 sccm to 0.4 at the mass flow rate of 0.73 $sccm$. It can also be observed that as the mass utilization efficiency increases from 0.3 to 0.7, the coupling coefficient goes up by approximately 30%. In Fig. 24 the same parameters are plotted for the Q factor of the thruster. Contrarily to the coupling factor, if we take the 0.2 $sccm$ case, the Q factor decreases by about 20% from the maximum of 70 to 55 with the increasing mass utilization efficiency until it starts to plateau at around 0.65 mass utilization efficiency. In this case, the Q factor can be treated as an indication of the coupling between the coil and the plasma: the larger the decrease in the thruster's Q factor, the larger the effect the plasma has on the coil.

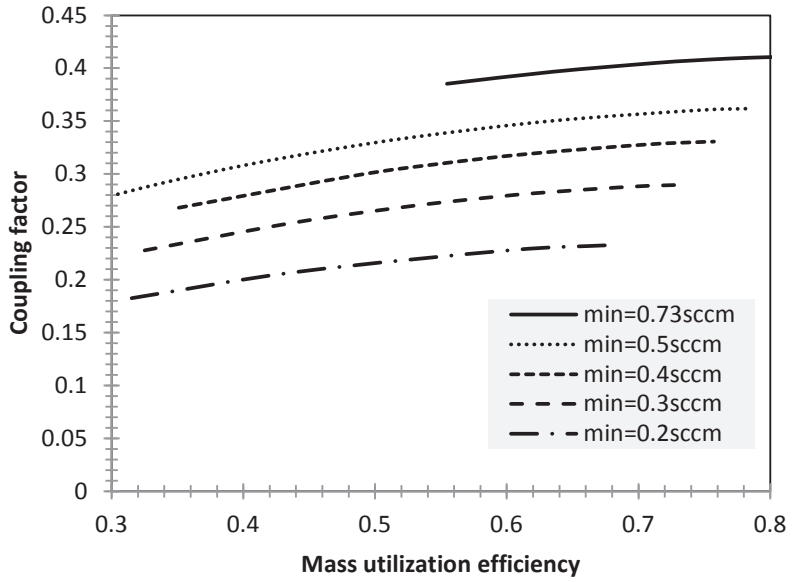

Figure 23. Coupling factor between the coil and plasma for different input mass flow rates.

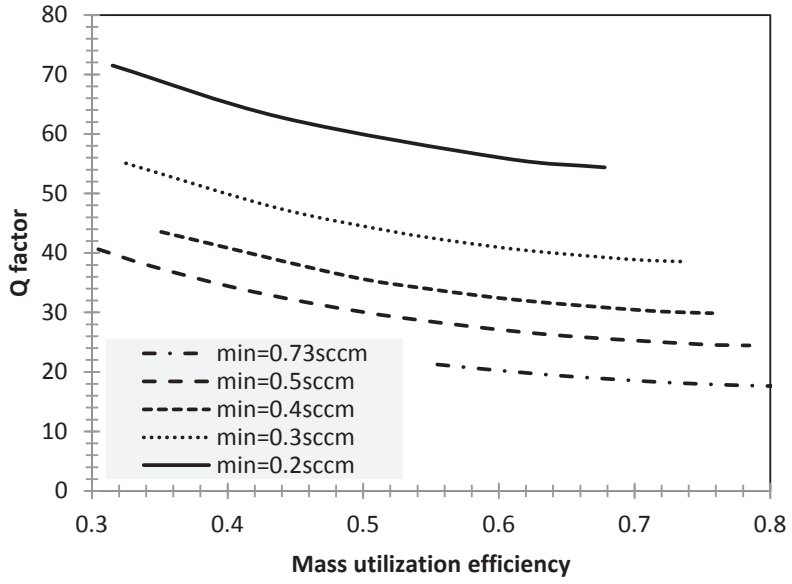

Figure 24. Thruster Q factor for different input mass flow rates.

Figure 25 highlights the heating mechanism inside the plasma of RIT 3.5 thruster. As can be seen, almost no power is transferred to the plasma sheath close to the wall since in this region the ion density is very low and, thus, the current density in negligible. The majority of plasma heating occurs in the vicinity of the plasma pre-sheath where the plasma density ratio h is about equal to h_r. Furthermore, the power absorption drops sharply upstream of the sheath edge since the current density starts decreasing. This is due to the plasma screening effect close to the coil surface at the radial edge of the discharge chamber.

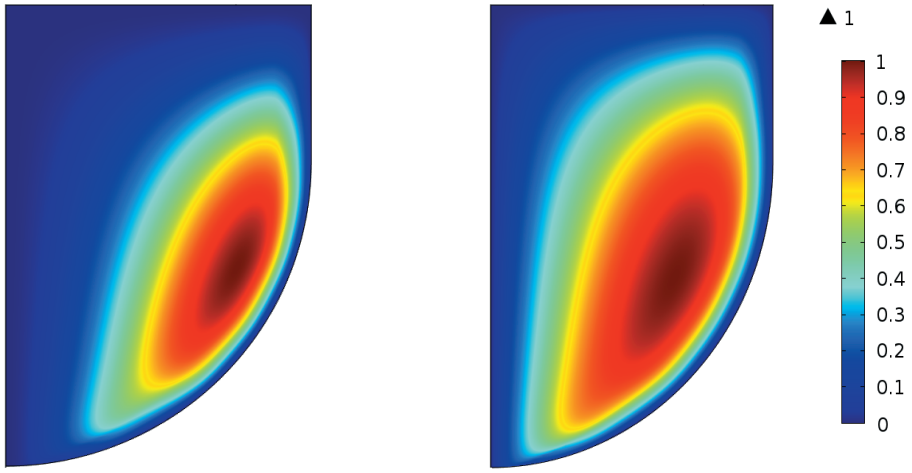

Figure 25. Electromagnetic power deposition (left) and current density (right) normalized to the maximum value in RIT 3.5 thruster for $2.5\ mN$ thrust operational condition.

As a first step in the thermal validation process it was decided to compare the model results to the thermal measurement data obtained without the plasma to exclude the possibility of a wrong plasma model and concentrate solely on the accuracy of the thermal model itself. Figure 26 displays the relative comparison between the temperatures measured in the experiment and those obtained in the model for the input power of $18\ W$. The largest discrepancy is observed in the temperature measured on the C_1 capacitor, which is about $8\ K$ or nearly 8% lower from the measured value. Other temperatures have similar percentage deviations. Figure 27 shows the temperature distribution surface plot for the same $18\ W$ input power case. The maximum temperature reached is 123 ℃ on the coil surface, while the C_1 capacitor temperature is 105 ℃.

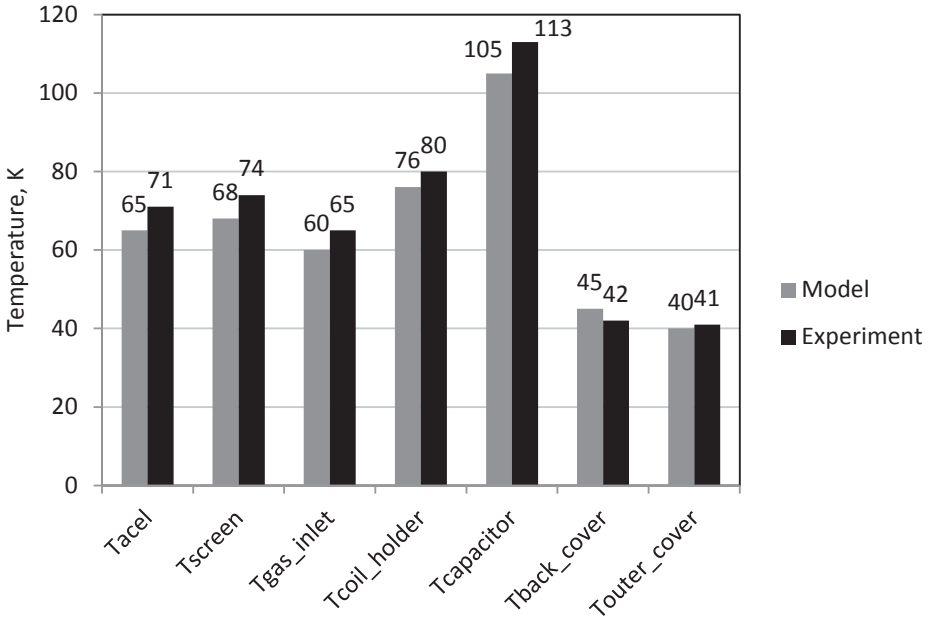

Figure 26. Temperature measurements without plasma for an input power of $18\ W$.
The meaning of the temperature measurements is indicated below the data.

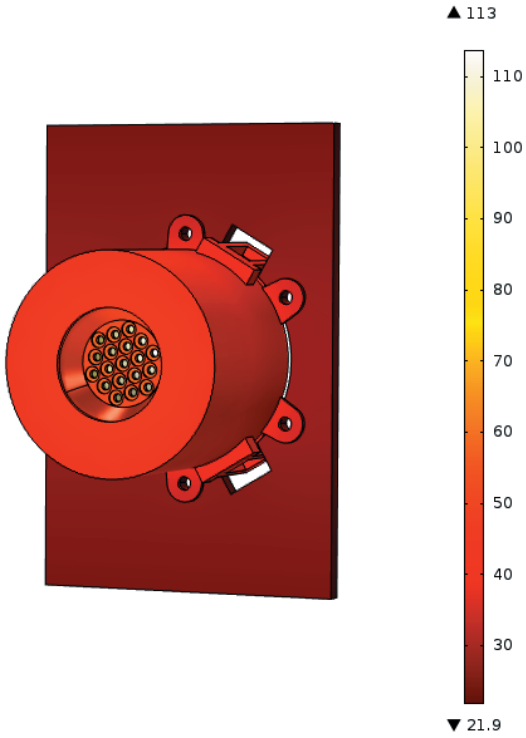

Figure 27. Temperature distribution for 18 *W* input power in RIT 3.5 thruster on the outside surfaces.

IV. Conclusion

A comprehensive radio frequency gridded-ion thruster model was presented that includes main aspects of the thruster operation. Different types of physics were represented with a different sub-model: 2D ion optics, 3D neutral gas, Boltzmann electron transport, 0D plasma, RF circuit, 2D electromagnetic and 3D thermal. A particular emphasis was placed on the accurate modeling of plasma conductivity. This included a correct representation of the ion density distribution, evaluation of the effective HF collision frequency and inclusion of the stochastic heating mechanism. Furthermore, thermal effects on the thruster component conductivity and neutral gas pressure were included as well. The model was benchmarked against the experimental results of RIT 3.5 thruster. It was shown that the model can predict the total input power and current with an error of less than 7%. Furthermore, the thermal model results were compared to the experimental results obtained by running the thruster with 18 *W* of input power without plasma. The thermal model was capable of predicting the temperature distribution within 10% error. The future aims include introducing an even more detailed description of the ion density distribution in the discharge, as well as performing a more thorough analysis of the magnetic field effects on the plasma confinement. The ultimate goal is to employ the model in designing and optimizing an RF thruster, as well as to perform plasma measurements to improve on the model assumptions.

References

[1]Groh, K. and Loeb, H., "State-of-The-Art of Radio-Frequency Ion Thrusters," *Journal of Propulsion and Power*, Vol. 7, No. 4, 1991, pp. 573-579.

[2]Leiter, H., Killinger, R., Bassner, H., and Müller, H., "Development and Performance of the Advanced Radio Frequency Ion Thruster RIT-XT," Presented at the *28th International Electric Propulsion Conference*, Toulouse, Mar 17-21, 2009.

[3]Leiter, H., Ellerbrock, H., and Feili, D., et. al., "Development of a Miniaturized RF Ion Engine System for Commercial and Scientific Applications," Presented at the *47th AIAA/ASME/SAE/ASEE Joint Propulsion Conference & Exhibit*, San Diego, CA, July 31-August 03, 2011.

[4]Feili, D., "μNRIT-2.5 - a New Optimized Microthruster of Giessen University," Presented at the *31st International Electric Propulsion Conference*, Ann Arbor, MI, September 20-24, 2009.

[5]Lotz, B., "Plasma Physical and Material Physical Aspects of the Application of Atmospheric Gases as a Propellant for Ion-Thruster of the RIT-Type," Ph.D. Dissertation, Justus-Liebig-University, Giessen, 2013.
[6]Lieberman, M., and Lichtenberg, A., *Principles of Plasma Discharges and Materials Processing*, 2nd ed., John Wiley & Sons, New Jersey, 2005.
[7]Piejak, R. B., Godyak V. A., and Alexandrovich, B. M., "A Simple Analysis of an Inductive RF Discharge", *Plasma Sources Sciences and Technology*, Vol. 1, No. 3, 1992, pp. 179-186.
[8]Chabert, P., and Braithwaite, N., *Physics of Radio-Frequency Plasmas*, Cambridge University Press, England, UK, 2011.
[9]Meng-Tsuan Tsay M., "Numerical Modelling of a Radio-Frequency Micro Ion Thruster," MSc Dissertation, MIT, MA, 2006.
[10]Volkmar C., and Ricklefs U., "Modeling of Electrical Parameters of an Inductively-Coupled Plasma Generator in 3-Dimensional Cartesian Space", *Proceedings of 2014 Space Propulsion Conference*, Cologne, 2014.
[11]Goebel, D., and Katz, I., *Fundamentals of Electric Propulsion*, John Wiley & Sons, Hoboken, NJ, 2005.
[12]Gartner, W., Lotz, B., and Meyer B. K., "3D Thermal Simulation of a uN-RIT," Presented at the *33rd International Electric Propulsion Conference*, Washington, US, October 6-10, 2013.
[13]COMSOL, Multi-Physics Software Package, Ver. 5.0.1.276, Southampton, 2015.
[14]PSPICE, Electronics Circuit Modeling Software Package, Ver. 9.1, Southampton, 2015.
[15]Matlab, Computation Software Package, Ver. 2014a, Southampton, 2015.
[16]Feili, D., Smirnova M., and Dobkevicius, M., et. al., "Design, Construction and Testing of a Radio Frequency Mini Ion Engine According to the Propulsion Requirements of the Next Generation Gravity Missions "NGGM"," Presented at the *30th ISTS, 34th IEPC and 6th NSAT Joint Conference,* Kobe-Hyogo, July 4 – 10, 2015.
[17]Brophy, J. R., Katz, I., Polk, J. E., and Anderson, J. R., "Numerical Simulations of Ion Thruster Accelerator Grid Erosion," Presented at the *38th AIAA/ASME/SAE/ASEE Joint Propulsion Conference & Exhibit*, July 7-10, Indianapolis, IN, 2002.
[18]Wang J., Polk J. E., Brophy J. R., and Katz I., "Three-Dimensional Particle Simulations of NSTAR Ion Optics," Presented at the *27th International Electric Propulsion Conference*, Pasadena, CA, October 15-19, 2001.
[19]Farnell C., "Performance and Life Simulation of Ion Thruster Optics," Ph.D. Dissertation, Colorado State University, Fort Collins, CO, 2007.
[20]Clausing, P., "The Flow of Highly Rarefied Gases Through Tubes of Arbitrary Length," *Journal of Vacuum Science and Technology*, Vol. 8, No. 5, 1971, pp. 636–646.
[21]Lister, G., Li, Y., and Godyak, V., "Electrical Conductivity in High-Frequency Plasmas," *Journal of Applied Physics*, Vol. 79, No. 12, 1996, pp. 8993-8997.
[22]Hagelaar G.J.M., and Pitchford L.C., "Solving the Boltzmann Equation to Obtain Electron Transport Coefficients and Rate Coefficients for Fluid Models", *Journal of Plasma Sources Science and Technology*, Vol. 14, No. 4, 2005, pp. 722-733.
[23]Meunier, J., Belenguer, Ph., and Boeuf J.P., Numerical Model of an AC Plasma Display Panel Cell in Neon-Xenon Mixtures", *Journal of Applied Physics*, Vol. 78, No. 2, 1995, pp. 731-745.
[24]Schäfer, M., "Plasma Diagnostic in RIT 10 Ion Thruster, " or "Plasmadiagnostik und Energiebilanzunterscuhung an dem HF-Ionentriebwerk RIT 10," Ph.D. Dissertation, University of Giessen, Giessen, 1971.
[25]Shkarofsky, I., Johnston, T., and Bachynski, M., *The Particle Kinetics of the Plasmas*, Addison-Wesley, 1996.
[26]Godyak V. A., Piejak R. B., and Alexandrovich B. M., "Experimental Evidence of Collisionless Power Absorption in Inductively Coupled Plasma," *Physical Review Letters*, Vol. 80, No. 15, 1998, pp. 3264-3267.
[27]Turner M.M., "Collisionless Electron Heating in an Inductively Coupled Discharge," *Physical Review Letters*, Vol. 3, No 9, 1997, pp. 3163-3166.
[28]Van Noord, J., "NEXT Ion Thruster Thermal Model," Presented at the 43rd *Joint Propulsion Conference and Exhibit,* Cincinnati, OH, July 8-11, 2007.